# Induction and quantification of cellulose nanofibril alignment in nano-hydroxyapatite biocomposite films

Sahar Roozbahani
  University of Maine System

Joshua Hamilton
  University of Maine System

Omar Alsamsam
  University of Maine System

Michael Mason
  University of Maine System

Karissa Beth Tilbury  ( ✉ karissa.tilbury@maine.edu )
  University of Maine System   https://orcid.org/0000-0003-0841-1077

# Abstract

Cellulose nanofibrils (CNFs) have been explored as an emerging naturally sourced material for the development of new biomaterials. The ability to reproducibly tune CNF fiber alignment is an active area of CNF-based biomaterial research. Typically, CNF-based biomaterials are composites, requiring the ability to control the organization of both CNF and additional additives to achieve desired mechanical and cellular interactions. Here, we present a simple CNF fibril alignment strategy based on the application of constant unilateral force on thin CNF films drying on a flexible substrate to reproducibly modulate CNF fibril alignment while integrating nanoparticle hydroxyapatite, a candidate mineral oxide. CNF fibril alignment/orientation is characterized using Polarized Light Microscopy (PLM), Scanning Electron Microscopy (SEM) and mechanical tensile testing. Collectively, all these characterization tools demonstrate that the application of a 10.2 N unilateral force on a CNF film drying on a flexible substrate results in increased CNF fibril alignment. Furthermore, the addition of nanoparticle hydroxyapatite did not diminish the CNF fibril alignment as assessed by both PLM, SEM, and modulus of elasticity highlighting the utility of the CNF film fabrication technique. In summary, the application of unilateral force on thin CNF films adhered to latex is an elegant, scalable, and cost-effective technique for generating CNF composite films with reproducible fibril alignment.

# Introduction

Biopolymers are known to have superior biocompatibility compared to synthetic polymers and their nontoxic nature suits tissue engineering applications (Lin and Dufresne 2014; Alini et al. 2019; Sharip and Ariffin 2019; Seddiqi et al. 2021). Cellulose is a primary component of every plant cell wall and is the most abundant polymer on earth. Cellulose nanofibrils (CNFs) are a cellulose derivative which is primarily produced using chemical and mechanical treatments on wood pulp or agricultural waste (Manian et al. 2021). CNFs can also be produced as an extracellular biosynthetic product from bacteria (Mohite and Patil 2014). Aquatic organisms such as algae and tunicates are examples of marine sources of CNFs (Wahlström et al. 2020; Pennells et al. 2020). Isolated CNFs have high aspect ratios, diameters of 3−10 nm and 0.5−2 microns long (Ansari and Berglund 2016). CNFs offer a diverse range of properties including crystallinity, high specific area, anisotropy, barrier properties, and chemical reactivity (Alini et al. 2019; Sharip and Ariffin 2019; Seddiqi et al. 2021). From a biological standpoint, they also benefit from critical features such as biocompatibility, biodegradability, and lack of toxicity as a biopolymer (Mohite and Patil 2014; Lin and Dufresne 2014; Alini et al. 2019; Pennells et al. 2020). CNFs are known for their outstanding mechanical properties and reinforcing characteristics (Ansari and Berglund 2016; Mokhena et al. 2021). The anisotropic character of CNF can lead to fiber orientation, impacting CNF's modulus of elasticity and tensile strength (Li et al. 2021). In nature, cellulose fibrils are present in the outer cell wall layer of plants and are naturally aligned to create a strong and durable structure (Ye et al. 2020).

CNFs are widely used in biomedical applications and several reviews highlight current and potential biomedical applications of CNFs from various sources (Lin and Dufresne 2014; Alini et al. 2019; Sharip and Ariffin 2019; Khalil et al. 2020; Moohan et al. 2020; Seddiqi et al. 2021). Some of the major

biomedical applications include: 1) tissue engineering, (Alini et al. 2019; Luo et al. 2019) 2) wound healing, (Fu et al. 2013; Gonzalez et al. 2014; Hakkarainen et al. 2016; Bacakova et al. 2019; Portela et al. 2019) and 3) drug delivery (Hasan et al. 2020; Liu et al. 2021; Raghav et al. 2021). Creation of bone scaffolds is a particularly promising tissue engineering area due to the tunability of the CNF mechanical properties to match mechanical properties of native human bone (Li et al. 2012; Garai and Sinha 2014; Eftekhari et al. 2014; Park et al. 2015; Huang et al. 2017). The size-scale of CNFs coupled with the ability to modify their bioactivity via surface chemistry (Eftekhari et al. 2014; Zhang et al. 2015; Huang et al. 2017) or the addition of other bioactive components such as hydroxyapatite in composite biomaterials (Li et al. 2012; Park et al. 2015; Ao et al. 2017; Daugela et al. 2018; Abouzeid et al. 2018) offer an exciting opportunity to mimic the extracellular matrix organization of bone tissue for the development of engineered bone scaffolds (Daugela et al. 2018).

Within tissue engineering applications, modulating the mechanical properties of the engineered scaffold is critically important. Controlling the degree of fiber alignment in CNF-based engineered constructs positively correlates with mechanical properties (Li et al. 2021). Beyond mechanical properties, cellular interactions such as cell polarity and cell elongation are directly influenced by fiber alignment of the contact surface (Kim et al. 2012; Wickström and Niessen 2018). For instance, CNF based tissue scaffolds fabricated by electro-spinning have demonstrated enhanced cell alignment leading to altered cell behavior including significantly affecting cell behavior including differentiation and adhesion (Chahal et al. 2014; He et al. 2014; Ao et al. 2017).

Bone possesses a hierarchical and anisotropic structure composed of collagen fibers and hydroxyapatite mineral (Reznikov et al. 2014). Currently, most bone regenerative treatments focus on increasing bone mass, while taking advantage of the native oriented structure in the bone scaffold (Dimitriou et al. 2011). The limited availability of suitable cadaver has inspired the exploration of engineered alternatives. Mimicking the oriented extracellular matrix (ECM) structure of natural bone remains challenging. Previous work has demonstrated that manipulating the scaffold morphology promotes proliferation and differentiation of osteoblasts to osteocytes to more closely mimic the natural bone regeneration process (Torres-Rendon et al. 2015; Lee et al. 2017). Additionally, the inclusion of nanoparticulate HA has been shown to enhance bioactivity resulting in improved integration of implants with surrounding tissue (Mucalo 2015). Therefore, targeted exploration of methods that combine the benefits of HA inclusion and fiber alignment to reproducibly modulate fiber alignment in the presence of HA are needed to more effectively mimic natural bone structure and composition.

Fiber alignment can be achieved by various techniques including vacuum filtration, (Ghasemi et al. 2020) electromagnetic (EM) fields, (Kim et al. 2008; Zhang et al. 2015) and hydrodynamic alignment (Håkansson et al. 2016). Although these methods are effective, the underpinning physics limit their applications. For example, electromagnetic methods restrict the development of composites as the additional material must have similar dipole characteristics as CNF to avoid separation. This limits the use of electromagnetic methods in generating a CNF/mineral oxide composite material with homogenous distribution of mineral oxides within the network for increased stiffness and

biocompatibility. Similarly, hydrodynamic alignment methods require precise control of fluid viscosity and nozzle velocity and are generally not well suited for high concentration suspensions (Håkansson et al. 2014, 2016). In thin-film polymer science, it is common to dry films on an impermeable substrate. Here the fiber orientation is directed by internal forces exerted on individual fibers due to contraction during drying. Recently, Tajvidi and colleagues demonstrated modest CNF alignment using this technique; however, the method has limited tunability due to rapid dewatering from the initial vaccum filtration step. This limits the impact of the stretching forces to facilitate hydgrogen-bonding and create more aligned nanofibrils. The ability to modulate the extent of CNF alignment is needed to achieve the mechanical properties and elicit cellular interactions cellular interactions (Ghasemi et al. 2020). Furthermore, most of these methods have only been applied to pure CNFs, their feasibility for CNF composites are yet to be explored.

To aid in the development and characterization of CNF/HA composite materials, a non-destructive technique with sensitivity of fiber alignment is required. The method described here is based on the application of a controllable unilateral force applied via a deformable latex substrate during the CNF drying process to create orientated CNF films. Additionally, reducing the water content of the starting CNF suspension increases the adhesion of the CNF slurry to the latex substrate enabling even greater transmission of the alignment force. The utility of this method for fiber orientation in more complex CNF-composite films was also explored with up to 10% (dry basis) mineral additives (hydroxyapatite). Here, we used Polarized Light Microscopy (PLM) and the innate birefringence of CNF to spatially map the degree of fiber orientation using the Birefringence Orientation Index (BOI) in a custom ImageJ macro. Scanning Electron Microscopy (SEM) images corroborated the aligned network of CNFs within the biocomposites at the surface and tensile tests confirmed internal alignment of CNFs. Therefore, we conclude that use of BOI is an appropriate non-destructive screening tool for the characterization of CNF alignment in the formulation of new CNF biocomposites.

## Experimental Section

All films were prepared using CNF suspensions in water (3 wt%), obtained from the University of Maine Process Development Center (PDC) prepared from chemically bleached northern softwood pulp by mechanical refining. The CNF used in this study was previously characterized by our colleagues at the University of Maine and the average fiber diameter was $20-500$ nm (Mazhari Mousavi et al. 2017). Hydroxyapatite (HA) in water (15 wt%) and particle size of less than 50 nm was purchased from Sigma Aldrich with the surface area$\geq 80$ $m^2$/g and used without modification. Latex bands, used routinely for physical therapy (Thera-Band, 4.6 lbf @ 100% elongation), were implemented without modification as the deformable substrates for this study.

Thin film preparation

The stock 3 wt% CNF suspension was diluted to 1.5 wt% solids in distilled water to decrease the viscosity and ease the spread of the CNF solution. Nine grams of the resulting CNF suspension was spread using a standard laboratory spatula on a 2 x 5-inch latex band. The latex band was taped on all edges to a hard

flat rigid surface to ensure constant tension in the latex band and avoid dripping of the approximately 1 mm thick CNF films. These samples were left to dry in ambient room conditions overnight and were labeled as "unstretched". The "stretched" pure CNF films were prepared following the same deposition process as above but were placed under a box (STP) to reduce air flow for 3 hours to decrease the sample moisture content by approximately 30% (by weight). The reduction in moisture content increases adhesion sufficiently to allow for both the latex substrate and the CNF film to be stretched during drying. At this stage, the latex band was stretched lengthwise by applying a controlled force to one end while the other end was fixed (Fig. 1). The samples were left to dry at STP conditions overnight. The hydroxyapatite/CNF composite films were fabricated in the same way but with the addition of HA paste to the CNF suspension with a 1:10 weight ratio, followed by magnetic stirring at 200 rpm for 4 hours, to ensure adequate dispersion of the HA into the CNF network. Dried films were carefully peeled off the latex and stored with silica beads in sealed plastic bags for further characterization. To achieve the highest level of orientation and to determine the effect of an applied force on fiber alignment, a series of samples were prepared with applied forces ranging from 0 to 11.1 kN.

Polarized light microscopy

Polarized light microscopy (PLM) was used to map the fiber orientation of the prepared films. A standard Olympus IX73 inverted microscope, equipped with a 10X 0.4NA air objective and Amscope color (CMOS) camera was used for imaging of all samples. Two broadband linear polarizers were crossed above and below the sample stage thereby eliminating all light transmission. A 530 nm full-wave retardation plate was fixed in a 360° rotation mount above the stage but below the first polarizer. Using this configuration, commonly used in mineralogy, (Montana 2020) the wave plate introduces an optical path length difference of 530 nm for light of this same wavelength in the incident linearly polarized white light. The green photons (530 nm) therefore remain linearly polarized and are fully attenuated by the subsequent crossed polarizer, whereas all other wavelengths are elliptically polarized. As a result, all other wavelengths pass through the crossed polarizer combining to create magenta-red color using Newtonian color addition/subtraction. When a sample is introduced, the birefringence introduces a phase shift proportional to the interaction of the light relative to the optical axis of the birefringent material (Oldenbourg 2013). This interaction results in either positive or negative interference when combined in the analyzer of the PLM microscope resulting in blue (additive) or yellow (subtractive) colors. Images were acquired using a 2MP RGB, CMOS Amscope (MD200) eyepiece camera. Three samples of each type were tested, where 5 areas of each sample were imaged.

To obtain quantifiable isotropic information from the CNF films, control of the relative angles of orientation between the waveplate and the CNF sample orientation is required. Rectangular CNF films were fixed onto the microscope stage with the long axis (applied force axis, see Fig. 2) parallel to the horizontal edge of the stage. RGB images are acquired at both +/- 45° rotation of the 530 nm full wave retardation plate with respect to the stage-mounted sample to be used in the BOI analysis.

BOI analysis

Birefringence imaging is routinely used to map inhomogeneities in lithographic and biological samples (Burnett et al. 2001; Oldenbourg 2013). More recently, this common technique has been adapted, where specific digital color channels are used to enhance and quantify birefringence contrast, referred to as the Birefringence Orientation Index (BOI) (Ghasemi et al. 2020). Specifically, the BOI index relates the relative intensity of the red and blue color channels to the positive or negative birefringence of the sample.

The BOI analysis was performed with a custom image processing algorithm using ImageJ software (Schneider et al. 2012). The RBG images, at both +/-45°, were separated into their respective RGB color channels. The +/-45° green channel images were averaged together and used as a mask to reduce noise from the set-up due to the use of a 530 nm full wave retarder plate which extinguishes green wavelengths in the crossed polarizers in the absence of a sample. CNFs are birefringent material, therefore when probed with linear polarization, the birefringence of CNFs shift the interfering wave fronts in the crossed analyzer resulting in either blue or yellow interference colors (Ghasemi et al. 2020). All BOI calculations used the blue channel images. The blue channel images were filtered using the average of the +/-45° green channel images as a mask to remove noisy pixels and the 8-bit images. The masked images were rescaled 1-256 to eliminate 0 as a pixel value.

The BOI map was generated by using Eq. 1 where b is the pixel intensity of the blue channel at -/+45°. Resulting BOI maps were smoothed using a median filter with a radius of 3. The average BOI (Fig. 4b) of each film (n = 3) was based on the average BOI of 5 images of each film. A BOI value close to zero indicates no minimum to no alignment whereas values of − 1 and 1 represent maximum orientation.

$$BOI = \frac{b-45 - b+45}{b-45 + b+45} \quad (1)$$

Fiber Orientation Analysis

Surface morphology and fiber directionality were investigated by Scanning Electron microscopy (SEM); using a Zeiss NVision 40 Microscope. Three SEM micrographs of each sample were obtained at 3 KV with 1KX and 5KX magnification. The orientation of the fibers in the 1KX images were quantified using a sliding gaussian window method to calculate a local gradient structure tensor to quantify fiber orientation. This analysis was performed using OrientationJ (Püspöki et al. 2016). A histogram of fiber orientation was created using OrientationJ which classifies the fibers based on pixel coherency.

Mechanical Properties evaluation

Tensile tests were performed using an Instron universal testing machine (Model 5942, INSTRON Instruments, Norwood, MA, USA) with a 500 N load cell. Five samples of each type were cut into a standard the ASTM standard dog-bone shape with the gauge length of 20 mm (20 mm width and 10 mm width of the neck-down). The cross-head motion speed was adjusted to 2 mm/min. Both tensile modulus and tensile strength of the samples were calculated from the load−deflection curves.

Statistical Testing

Results of BOI analysis and mechanical properties were analyzed statistically using one-way analysis of variance (ANOVA), comparisons were made at 95% confidence level.

# Results And Discussion

BOI calculation

The linear relationship between applied longitudinal force and measured BOI is demonstrated in Fig. 2. The force is applied to the sample once the solution is well adhered to the latex substrate (after losing 30% of its initial water content). The amount of force applied to stretch the wet sample was quantified by measuring the maximum longitudinal force required to fully stretch the band without breaking the sample. For each weight applied, the amount of BOI was calculated accordingly. The results of the force optimization experiments indicate that the average BOI increased from -0.13 to -0.75 for pure CNF samples at maximum force applied. When the longitudinal force exceeded 10.2 N, the sample failed to form a continuous film, fractured and delaminated from the latex support material.

Fig. 3 shows representative PLM images of unstretched and stretched samples by applying maximum force (10.2N).  Unstretched samples had visual shifts in color due to CNF birefringence. The apparent color shift of the stretched CNF samples was generally dominated by a single color and appeared more uniform across the sample area indicating that the fibril structure of the CNFs are more uniformly arranged.

BOI maps generated using equation 1 are shown in Fig. 4A. Here negative and positive birefringence are represented by blue (-1) and red (+1), respectively. Both extremes indicate high fiber orientation whereas values closer to 0 indicate non-oriented samples. Highly oriented samples are expected to appear as dominantly blue or red depending on the degree of positive or negative birefringence. Fig. 4a shows that stretched samples have a blue dominant BOI close to -1. Representative BOI map and  film average BOI values are shown in Fig. 4a and 4b.  The box and whisker plots of the average BOI of the 3 independent CNF films (Fig. 4b) demonstrate that the stretched CNF films have an average BOI close to -1. This indicates that the CNF is aligned with similar dipole-dipole interactions due to the dominantly negative birefringence, whereas the unstretched CNF samples lack any dominant BOI feature.

The average BOI value for stretched films was -0.75; whereas the average BOI of unstretched samples had a value of -0.13, showing a significant increase (P<0.05) in birefringence, indicating greater fiber orientation. To demonstrate the robustness of this sample preparation method, HA was included in the initial slurry (10% by dry weight). The resulting PLM data suggest that the presence of HA did not significantly alter the BOI values relative to pure stretched CNF films as demonstrated by both the BOI image (P>0.05) Fig. 4a and 4b. The average BOI achieved for the stretched CNF/HA sample was -0.77, comparable to the value of -0.75 obtained for the pure CNF sample.

To further support that the BOI method is sensitive to CNFs fiber orientation, 3 SEM images of each film type (unstretched CNF, stretched CNF, unstretched CNF/HA, and stretched CNF/HA acquired at 1KX magnification, were analyzed using the OrientationJ plugin in ImageJ to quantify the orientation of individual fibers. Polar plots of the fiber angles calculated using OrientationJ are seen in Fig. 5 where the dominant fiber angle was normalized and centered at 0° for the unstretched, stretched, and HA-doped stretched CNF films. These data clearly indicate that fiber alignment in both the CNF and CNF/HA composite films exhibit increased alignment compared to the unstretched film.

Fig. 6 represents modulus of elasticity and tensile strength values of stretched and unstretched films. The results of the tensile test showed that the tensile modulus of both stretched pure CNF and stretched HA/CNF films significantly increased (P value < 0.05), which based on prior literature indicates internal alignment of fibers (Ghasemi et al. 2020). Interestingly, the addition of HA in both the stretched and unstretched samples significantly reduces the tensile strength (P value <0.05) likely due to the HA nanoparticulate disrupting the hydrogen bonding between CNFs. Interestingly, the tensile strength for the composite CNF/HA material approached the tensile strength of unstretched CNF films. The elastic modulus is significantly increased for stretched CNF films (p value <0.05 and there was no significant difference between the modulus of elasticity of stretched CNF and stretched CNF/HA films. This is in agreement with the previous data that both pure CNF and CNF/HA films had the same BOI value suggesting that they have same level of orientation. Collectively, the tensile strength and elastic modulus suggest application of longitudinal force results in internal alignment of CNFs.

## Conclusion

A novel, cost effective and tunable method to induce fiber orientation in CNF and CNF/HA films was developed. A BOI index method was adapted to compare PLM data which showed that our method significantly increased fiber orientation in both pure CNF and hydroxyapatite incorporated CNF films. Mechanical testing demonstrated increased tensile strength and modulus of elasticity of stretched films implying that the CNFs were internally aligned. SEM images were used to validate the BOI results and provide insight into the narrow orientation distribution for stretched samples compared to unstretched samples. Both PLM and SEM results showed that incorporating HA into the CNF matrix did not interfere with the fiber orientation or film consistency and they both showed fiber orientation. HA has been shown to improve bioactivity and biocompatibility of the films and its incorporation in a highly aligned oriented matrix achieved by our method can be particularly beneficial in bone regeneration studies.

## Declarations

**Competing Interests:** *The authors have no relevant financial or non-financial interests to disclose.*

# References

1. Abouzeid RE, Khiari R, Beneventi D, Dufresne A (2018) Biomimetic Mineralization of Three-Dimensional Printed Alginate/TEMPO-Oxidized  Cellulose Nanofibril Scaffolds for Bone Tissue Engineering. Biomacromolecules 19:4442–4452. https://doi.org/10.1021/acs.biomac.8b01325

2. Alini M, Ghosh S, Pelling AE, Hickey RJ (2019) Cellulose Biomaterials for Tissue Engineering. Front Bioeng Biotechnol | www.frontiersin.org 1:45. https://doi.org/10.3389/fbioe.2019.00045

3. Ansari F, Berglund LA (2016) Tensile Properties of Wood Cellulose Nanopaper and Nanocomposite Films. In: Multifunctional Polymeric Nanocomposites Based on Cellulosic Reinforcements. Elsevier Inc., Fibre and Polymer Technology, School of Chemical Science and Engineering (CHE), KTH, pp 115–130

4. Ao C, Niu Y, Zhang X, et al (2017) Fabrication and characterization of electrospun cellulose/nano-hydroxyapatite nanofibers for bone tissue engineering. Int J Biol Macromol 97:568–573. https://doi.org/10.1016/j.ijbiomac.2016.12.091

5. Bacakova L, Pajorova J, Bacakova M, et al (2019) Versatile Application of Nanocellulose: From Industry to Skin Tissue Engineering and Wound Healing. Nanomater (Basel, Switzerland) 9:164. https://doi.org/10.3390/nano9020164

6. Burnett JH, Levine ZH, Shirley EL (2001) Intrinsic birefringence in calcium fluoride and barium fluoride. Phys Rev B 64:241102. https://doi.org/10.1103/PhysRevB.64.241102

7. Chahal S, Fathima SJH, Yusoff MBM (2014) Biomimetic growth of bone-like apatite via simulated body fluid on hydroxyethyl cellulose/polyvinyl alcohol electrospun nanofibers. Biomed Mater Eng 24:799–806

8. Daugela P, Pranskunas M, Juodzbalys G, et al (2018) Novel cellulose/hydroxyapatite scaffolds for bone tissue regeneration: In vitro and in vivo study. J Tissue Eng Regen Med 12:1195–1208. https://doi.org/https://doi.org/10.1002/term.2651

9. Dimitriou R, Jones E, McGonagle D, Giannoudis P V (2011) Bone regeneration: current concepts and future directions. BMC Med 9:66. https://doi.org/10.1186/1741-7015-9-66

10. Eftekhari S, El Sawi I, Bagheri ZS, et al (2014) Fabrication and characterization of novel biomimetic PLLA/cellulose/hydroxyapatite  nanocomposite for bone repair applications. Mater Sci Eng C Mater

Biol Appl 39:120–125. https://doi.org/10.1016/j.msec.2014.02.027

11. Fu L, Zhang J, Yang G (2013) Present status and applications of bacterial cellulose-based materials for skin  tissue repair. Carbohydr Polym 92:1432–1442. https://doi.org/10.1016/j.carbpol.2012.10.071

12. Garai S, Sinha A (2014) Biomimetic nanocomposites of carboxymethyl cellulose-hydroxyapatite: novel three  dimensional load bearing bone grafts. Colloids Surf B Biointerfaces 115:182–190. https://doi.org/10.1016/j.colsurfb.2013.11.042

13. Ghasemi S, Rahimzadeh-Bajgiran P, Tajvidi M, Shaler S (2020) Birefringence-based orientation mapping of cellulose nanofibrils in thin films. Cellulose 27:. https://doi.org/10.1007/s10570-019-02821-2

14. Gonzalez JS, Ludueña LN, Ponce A, Alvarez VA (2014) Poly(vinyl alcohol)/cellulose nanowhiskers nanocomposite hydrogels for potential wound dressings. Mater Sci Eng C 34:54–61. https://doi.org/https://doi.org/10.1016/j.msec.2013.10.006

15. Håkansson KMO, Fall A, Lundell F, et al (2014) Hydrodynamic alignment and assembly of nanofibrils resulting in strong cellulose filaments. Nat Commun 5:

16. Håkansson KMO, Lundell F, Prahl-Wittberg L, Söderberg LD (2016) Nanofibril Alignment in Flow Focusing: Measurements and Calculations. J Phys Chem B 120:6674–6686. https://doi.org/10.1021/acs.jpcb.6b02972

17. Hakkarainen T, Koivuniemi R, Kosonen M, et al (2016) Nanofibrillar cellulose wound dressing in skin graft donor site treatment. J Control Release 244:292–301. https://doi.org/10.1016/j.jconrel.2016.07.053

18. Hasan N, Rahman L, Kim S-H, et al (2020) Recent advances of nanocellulose in drug delivery systems. J Pharm Investig 50:553–572

19. He X, Xiao Q, Lu C, et al (2014) Uniaxially aligned electrospun all-cellulose nanocomposite nanofibers reinforced  with cellulose nanocrystals: scaffold for tissue engineering. Biomacromolecules 15:618–627. https://doi.org/10.1021/bm401656a

20. Huang Y, Wang J, Yang F, et al (2017) Modification and evaluation of micro-nano structured porous bacterial cellulose scaffold for bone tissue engineering. Mater Sci Eng C Mater Biol Appl 75:1034–1041

21. Khalil HPSA, Jummaat F, Yahya EB, et al (2020) A Review on Micro- to Nanocellulose Biopolymer Scaffold Forming for Tissue Engineering Applications. Polym.  12

22. Kim D-H, Provenzano PP, Smith CL, Levchenko A (2012) Matrix nanotopography as a regulator of cell function. J Cell Biol 197:351–360. https://doi.org/10.1083/jcb.201108062

23. Kim J, Chen Y, Kang K-S, et al (2008) Magnetic Field Effect for Cellulose Nanofiber Alignment. J Appl Phys 104:96104. https://doi.org/10.1063/1.3006140

24. Lee Y-J, An S-J, Bae E-B, et al (2017) The effect of thickness of resorbable bacterial cellulose membrane on guided bone regeneration. Materials (Basel) 10:320

25. Li K, Clarkson CM, Wang L, et al (2021) Alignment of Cellulose Nanofibers: Harnessing Nanoscale Properties to Macroscale Benefits. ACS Nano 15:3646–3673. https://doi.org/10.1021/acsnano.0c07613

26. Li K, Wang J, Liu X, et al (2012) Biomimetic growth of hydroxyapatite on phosphorylated electrospun cellulose nanofibers. Carbohydr Polym 90:1573–1581

27. Lin N, Dufresne A (2014) Nanocellulose in biomedicine: Current status and future prospect. Eur Polym J 59:302–325. https://doi.org/10.1016/J.EURPOLYMJ.2014.07.025

28. Liu Z, Zhang S, He B, et al (2021) Synthesis of cellulose aerogels as promising carriers for drug delivery: a review. Cellulose 28:2697–2714. https://doi.org/10.1007/s10570-021-03734-9

29. Luo H, Cha R, Li J, et al (2019) Advances in tissue engineering of nanocellulose-based scaffolds: A review. Carbohydr Polym 224:115144. https://doi.org/10.1016/j.carbpol.2019.115144

30. Manian AP, Cordin M, Pham T (2021) Extraction of cellulose fibers from flax and hemp: a review. Cellulose 28:8275–8294. https://doi.org/10.1007/s10570-021-04051-x

31. Mazhari Mousavi SM, Afra E, Tajvidi M, et al (2017) Cellulose nanofiber/carboxymethyl cellulose blends as an efficient coating to improve the structure and barrier properties of paperboard. Cellulose 24:. https://doi.org/10.1007/s10570-017-1299-5

32. Mohite B V, Patil S V (2014) A novel biomaterial: bacterial cellulose and its new era applications. Biotechnol Appl Biochem 61:101–110. https://doi.org/10.1002/bab.1148

33. Mokhena TC, Sadiku ER, Mochane MJ, et al (2021) Mechanical properties of cellulose nanofibril papers and their bionanocomposites: A review. Carbohydr Polym 273:118507. https://doi.org/https://doi.org/10.1016/j.carbpol.2021.118507

34. Montana G (2020) Ceramic raw materials: how to recognize them and locate the supply basins—mineralogy, petrography. Archaeol Anthropol Sci 12:. https://doi.org/10.1007/s12520-020-01130-1

35. Moohan J, Stewart SA, Espinosa E, et al (2020) Cellulose Nanofibers and Other Biopolymers for Biomedical Applications. A Review. Appl. Sci. 10

36. Mucalo MBT-H (Hap) for BA (ed) (2015) Index. In: Woodhead Publishing Series in Biomaterials. Woodhead Publishing, pp 375–381

37. Oldenbourg R (2013) Polarized light microscopy: principles and practice. Cold Spring Harb Protoc 2013:pdb-top078600

38. Park M, Lee D, Shin S, Hyun J (2015) Effect of negatively charged cellulose nanofibers on the dispersion of hydroxyapatite nanoparticles for scaffolds in bone tissue engineering. Colloids Surfaces B Biointerfaces 130:222–228

39. Pennells J, Godwin I, Amiralian N, Martin D (2020) Trends in the production of cellulose nanofibers from non-wood sources. Cellulose 27:. https://doi.org/10.1007/s10570-019-02828-9

40. Portela R, Leal CR, Almeida PL, Sobral RG (2019) Bacterial cellulose: a versatile biopolymer for wound dressing applications. Microb Biotechnol 12:586–610. https://doi.org/https://doi.org/10.1111/1751-7915.13392

41. Püspöki Z, Storath M, Sage D, Unser M (2016) Transforms and Operators for Directional Bioimage Analysis: A Survey. Adv Anat Embryol Cell Biol 219:69–93. https://doi.org/10.1007/978-3-319-28549-8_3

42. Raghav N, Sharma MR, Kennedy JF (2021) Nanocellulose: A mini-review on types and use in drug delivery systems. Carbohydr Polym Technol Appl 2:100031. https://doi.org/https://doi.org/10.1016/j.carpta.2020.100031

43. Reznikov N, Shahar R, Weiner S (2014) Bone hierarchical structure in three dimensions. Acta Biomater 10:3815–3826. https://doi.org/https://doi.org/10.1016/j.actbio.2014.05.024

44. Schneider CA, Rasband WS, Eliceiri KW (2012) NIH Image to ImageJ: 25 years of image analysis. Nat Methods 9:671–675. https://doi.org/10.1038/nmeth.2089

45. Seddiqi H, Oliaei E, Honarkar H, et al (2021) Cellulose and its derivatives: towards biomedical applications. Cellulose 28:1893–1931. https://doi.org/10.1007/s10570-020-03674-w

46. Sharip NS, Ariffin H (2019) Cellulose nanofibrils for biomaterial applications. Mater Today Proc 16:1959–1968. https://doi.org/10.1016/J.MATPR.2019.06.074

47. Torres-Rendon JG, Femmer T, De Laporte L, et al (2015) Bioactive gyroid scaffolds formed by sacrificial templating of nanocellulose and nanochitin hydrogels as instructive platforms for biomimetic tissue engineering. Adv Mater 27:2989–2995

48. Wahlström N, Edlund U, Pavia H, et al (2020) Cellulose from the green macroalgae Ulva lactuca: isolation, characterization, optotracing, and production of cellulose nanofibrils. Cellulose 27:3707–3725. https://doi.org/10.1007/s10570-020-03029-5

49. Wickström SA, Niessen CM (2018) Cell adhesion and mechanics as drivers of tissue organization and differentiation: local cues for large scale organization. Curr Opin Cell Biol 54:89–97. https://doi.org/10.1016/j.ceb.2018.05.003

50. Ye D, Rongpipi S, Kiemle SN, et al (2020) Preferred crystallographic orientation of cellulose in plant primary cell walls. Nat Commun 11:4720. https://doi.org/10.1038/s41467-020-18449-x

51. Zhang C, Salick MR, Cordie TM, et al (2015) Incorporation of poly(ethylene glycol) grafted cellulose nanocrystals in poly(lactic acid) electrospun nanocomposite fibers as potential scaffolds for bone tissue engineering. Mater Sci Eng C Mater Biol Appl 49:463–471. https://doi.org/10.1016/j.msec.2015.01.024
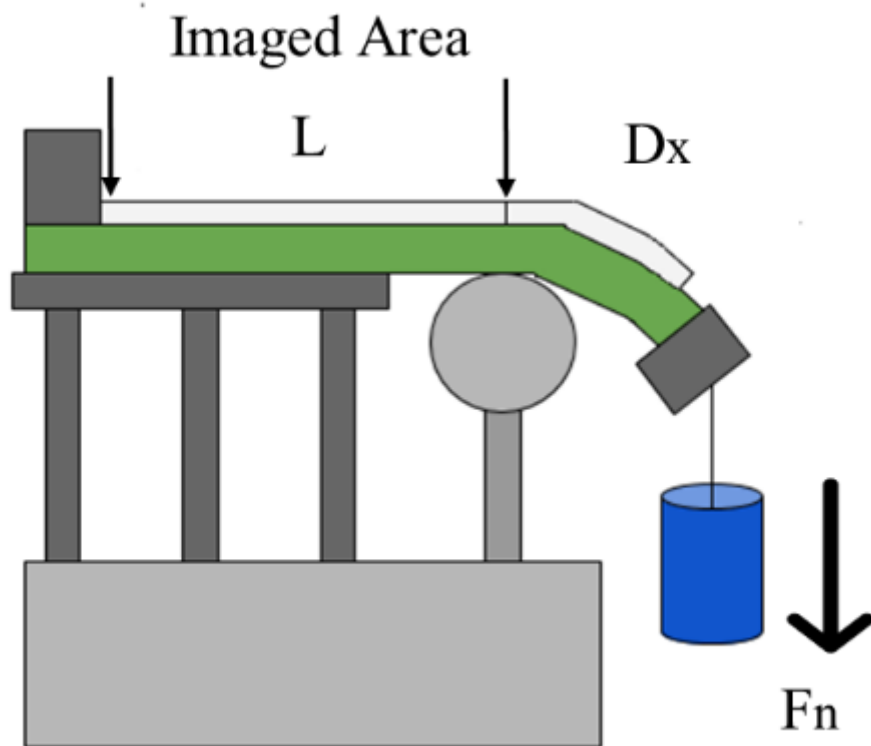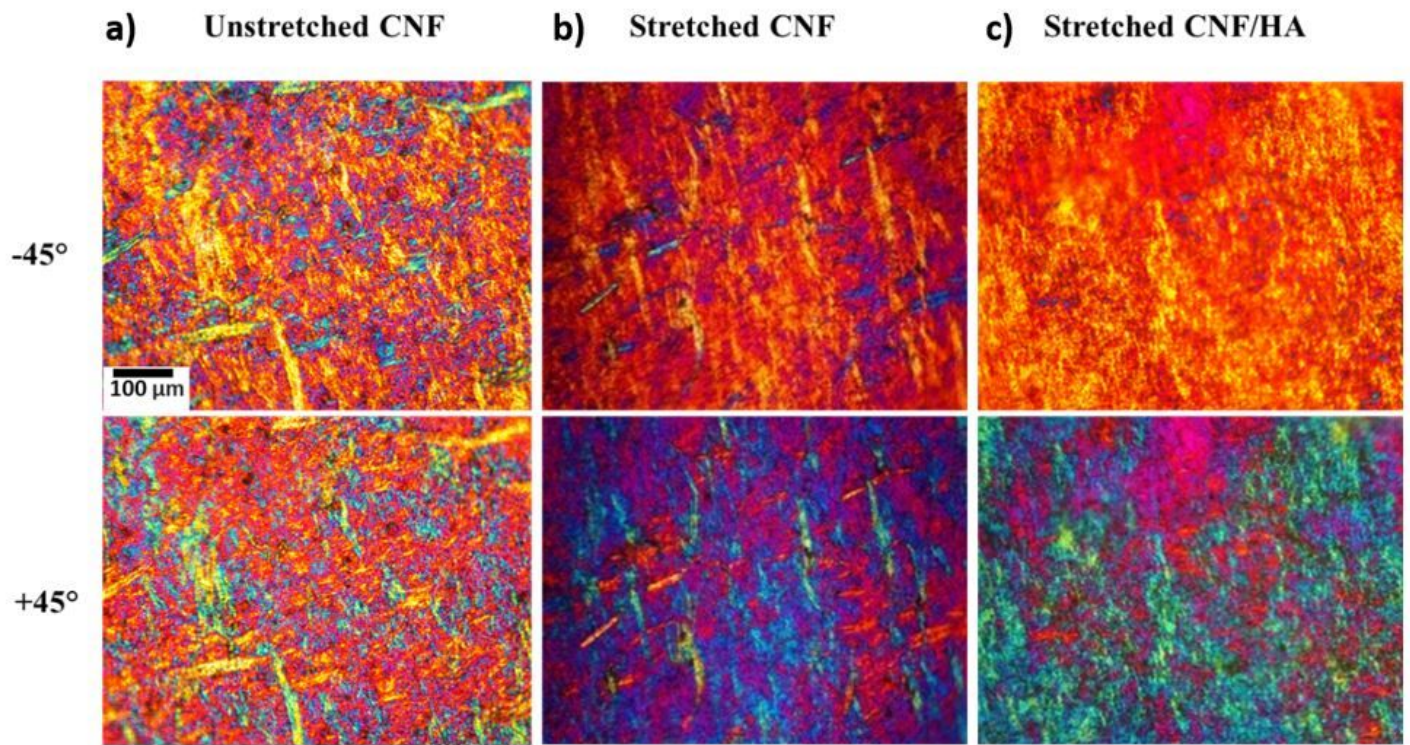
# Figures

**Figure 1**

Schematic of the unilateral stretching force apparatus for aligning CNF samples using constant uniaxial force
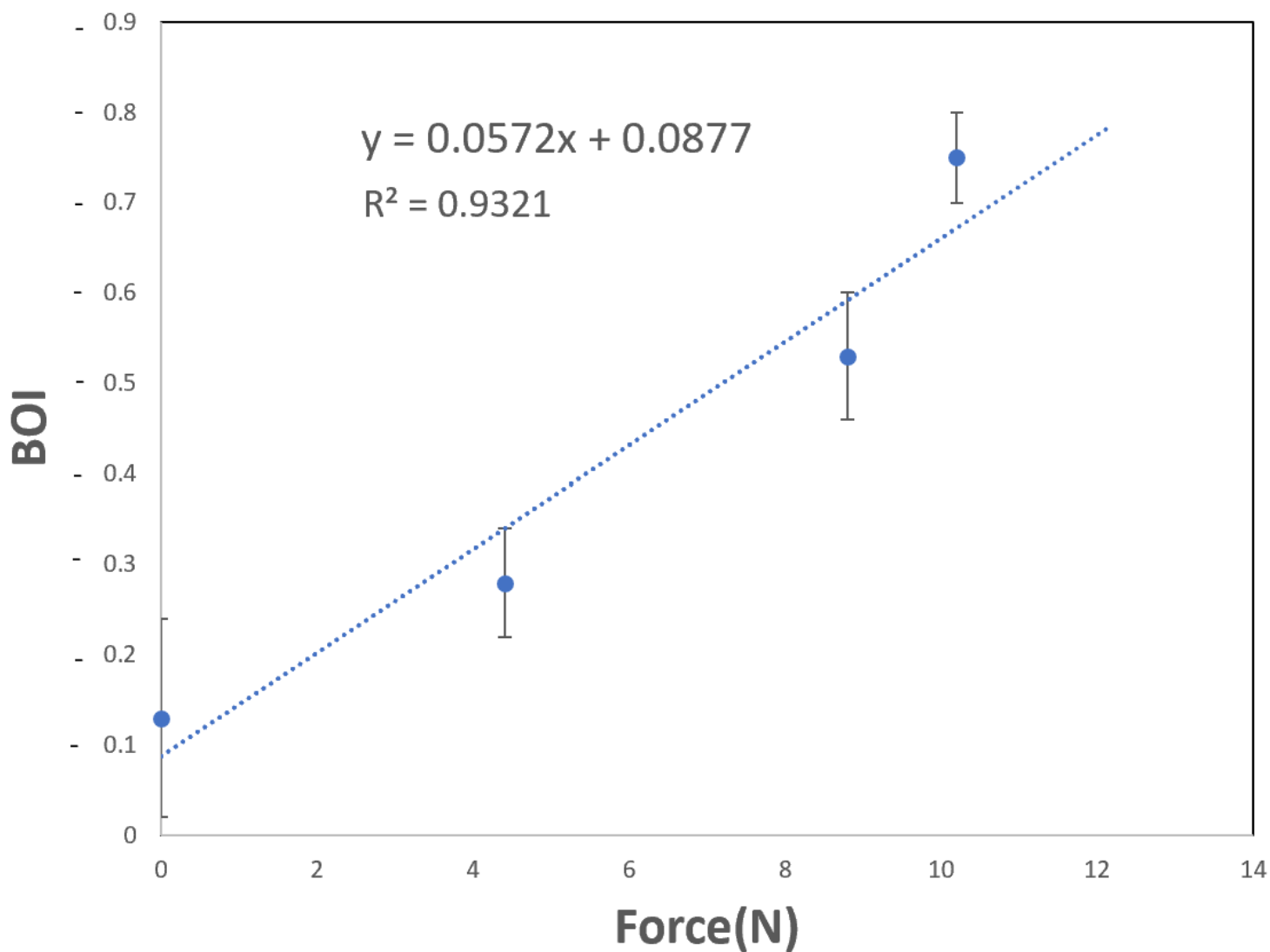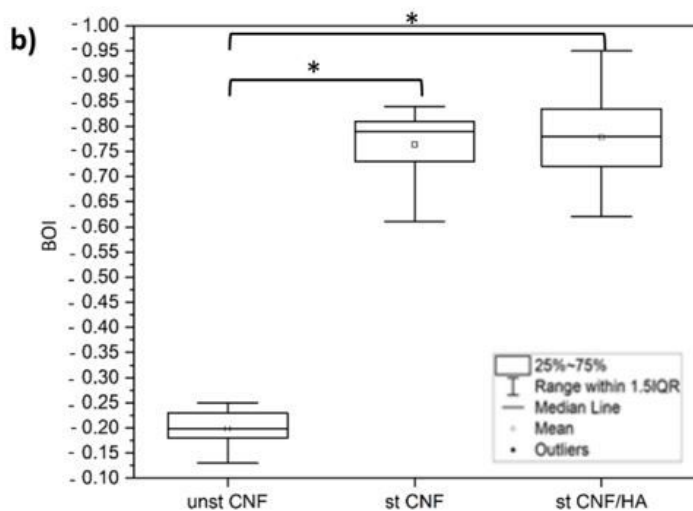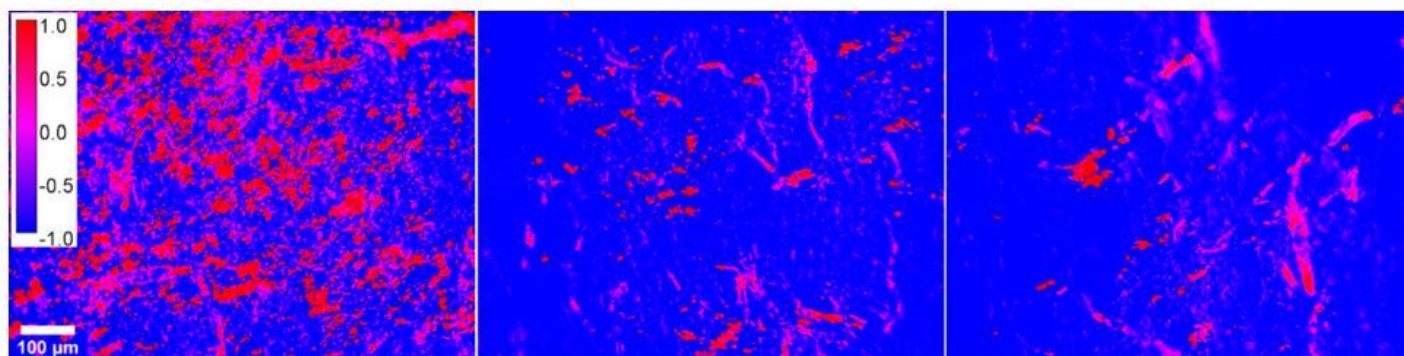
**Figure 2**

A linear regression of BOI as a function of applied force. Error bars represent standard deviation (n=3 films).
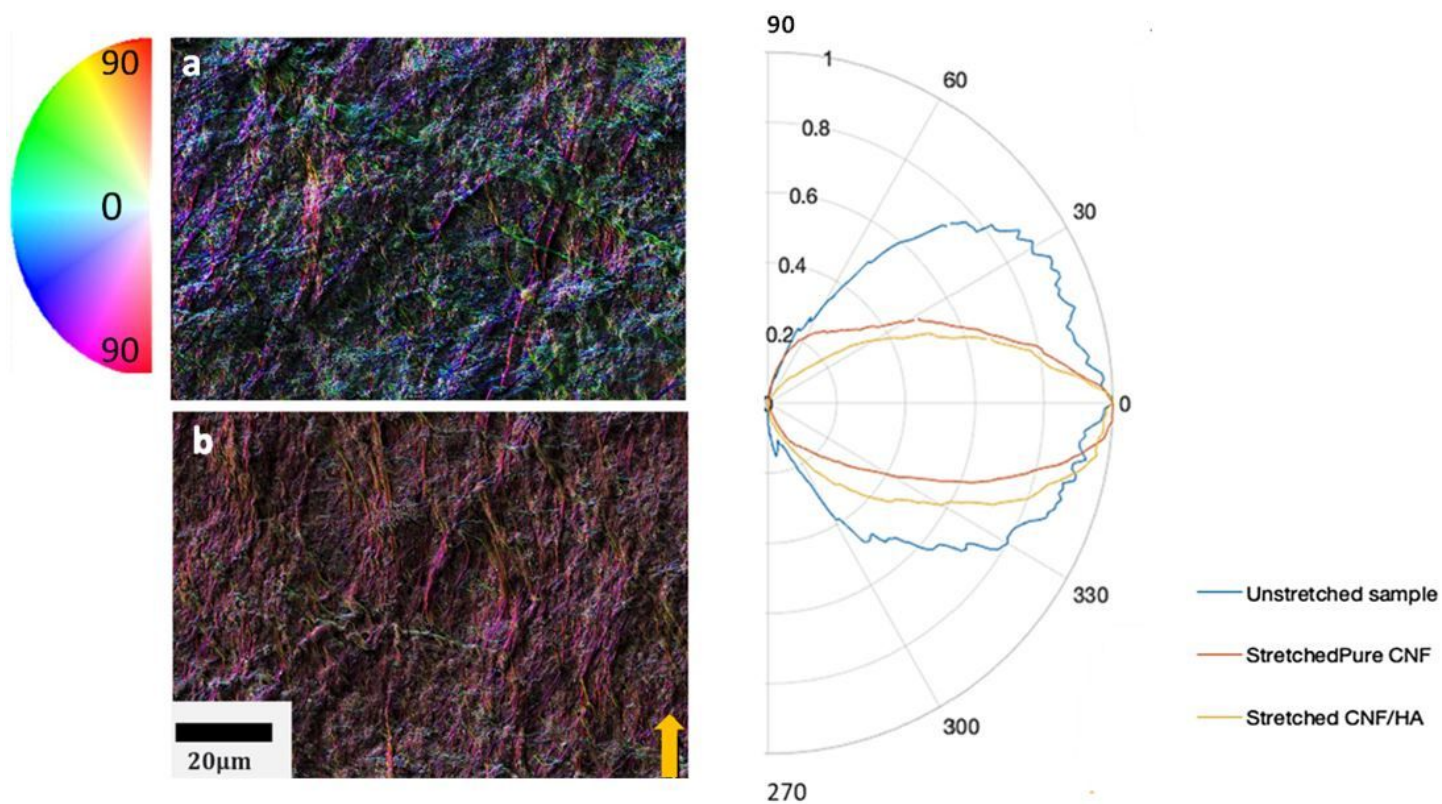
**Figure 3**

Raw representative PLM image set. Images acquired at -45°(top) and +45°(bottom) for a) unstretched and b) stretched and c) stretched CNF/nanohydroxyapatite samples.
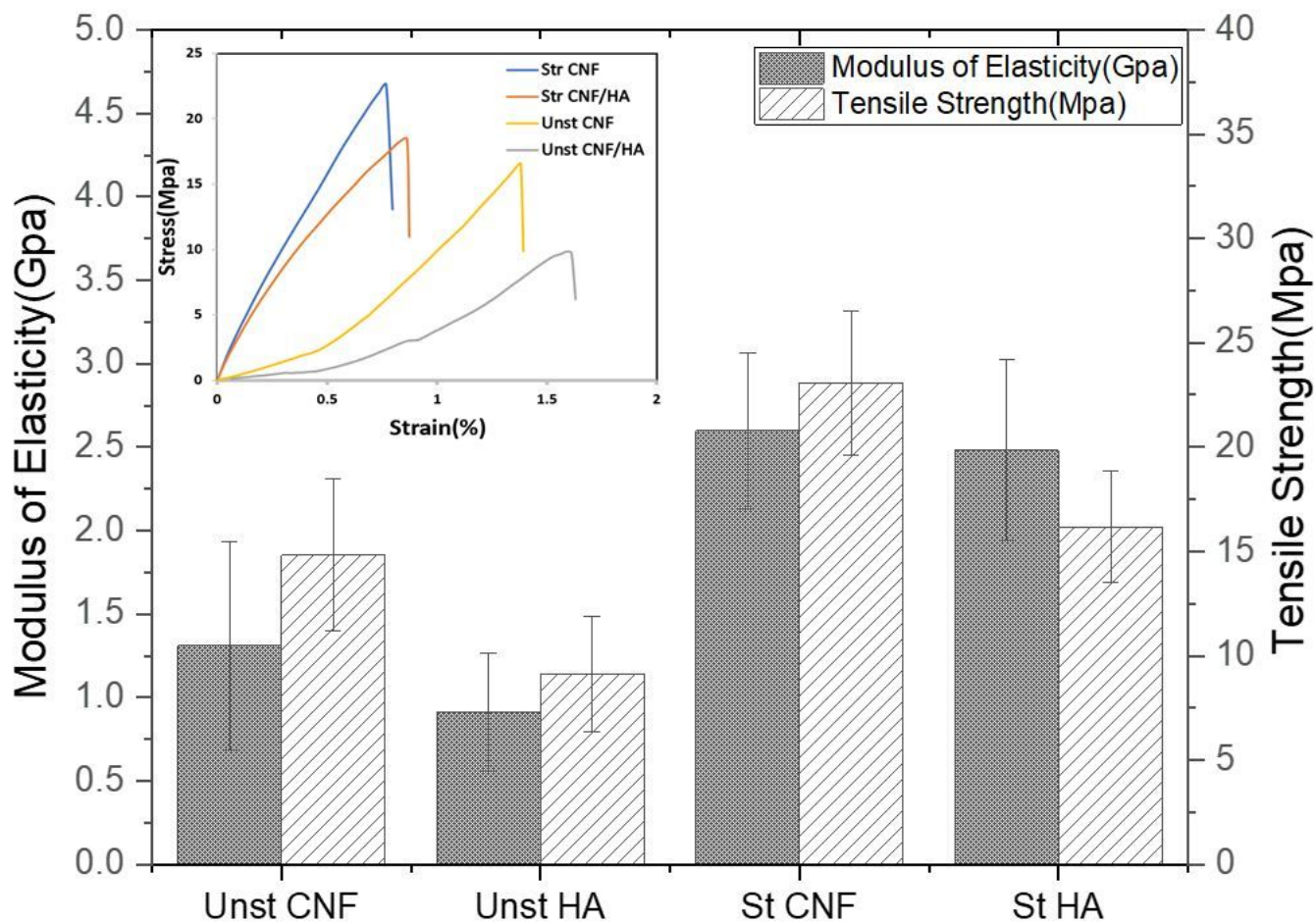
**Figure 4**

a) Representative BOI maps of stretched and unstretched samples. b) Comparison of average BOI values (n=3) of stretched and unstretched and stretched films. * indicates p < 0.05.

**Figure 5**

OrientationJ analysis results: a) Representative color-coded images of the surface of unstretched CNF film b) stretched CNF/HA film, yellow arrow shows the stretch direction C) Polar plot of fibril distribution of angles normalized around 0° for stretched and unstretched CNF samples (n = 3 films)

**Figure 6**

Tensile strength and modulus of elasticity of films (n=5). Inset is a single representative stress/strain curve of each of the sample types used to extract tensile strength and modulus of elasticity.